Theory-guided Sn/Cu alloying for efficient CO$_2$ electroreduction at low overpotentials

Xueli Zheng [1], Yongfei Ji[2,3], Jing Tang[1], Jiangyan Wang[1], Bofei Liu[1], Hans-Georg Steinrück[4], Kipil Lim[1,4], Yuzhang Li[1], Michael F. Toney[4], Karen Chan [3] and Yi Cui[1,5]*

Electrochemical CO$_2$ reduction to formate provides an avenue to reduce globally accelerating CO$_2$ emissions and produce value-added products. Unfortunately, high selectivity in formate electrosynthesis has thus far only been achieved at highly cathodic potentials. Here we use density functional theory to investigate the effect of alloying Cu and Sn on the activity and selectivity towards formate. A theoretical thermodynamic analysis of the reaction energetics suggests that the incorporation of copper into tin could suppress hydrogen evolution and CO production, thus favouring formate generation. Consistent with theoretical trends, the designed CuSn$_3$ catalysts by co-electrodeposition exhibit a Faradaic efficiency of 95% towards formate generation at −0.5 V versus RHE. Furthermore, the catalysts show no degradation over 50 h of operation. In situ Sn L$_3$-edge and Cu K-edge X-ray absorption spectroscopy indicate electron donation from Sn to Cu, which indicates positive oxidation states of Sn in CuSn$_3$ under operating conditions.

Electrochemical CO$_2$ reduction (CO$_2$RR) offers an appealing route to traditional pathways to fuels and chemicals[1–4]. While the technoeconomic viability of the direct electrosynthesis of multicarbon products requires significant reduction in overpotentials[5], the catalytic efficiencies and production rates for single-carbon products, such as CO and formate, provide more immediate opportunities for electrochemical CO$_2$ valorization[2,6,7].

Formate is a liquid fuel with high energy density, and is regarded as a useful hydrogen carrier for fuel cell applications[2,8,9]. However, the potential required for CO$_2$RR to formate with high selectivity is in general very high (−0.9 V versus reversible hydrogen electrode, RHE, with ~90% Faradaic efficiency)[8,10–14]. Catalysts including electrodes based on Cu[8,10], Sn[7,13], Pb[14], Pd[15] and Co[2] have each shown recent progress in CO$_2$RR to formate. Nevertheless, these catalysts still fail to meet strict criteria such as high selectivity at low overpotentials, and prolonged durability[9–11,13–15].

Sn-based catalysts have proven to have good selectivity for CO$_2$RR to formate[7,13,16,17]. However, they only exhibit good selectivity in a narrow and highly cathodic potential window[7,13,16,17]. Cu, although selective towards further reduced products at high overpotentials, also shows significant formate selectivity at low overpotentials[10]. Alloying as a means to tune selectivity has been exploited in several recent works. For example, CuAg alloys suppress hydrogen evolution and enhance the selectivity towards multi-carbon oxygenated selectivity[18], AuFe alloys increase CO selectivity and activity[19] and PdPt alloys show tunable formate selectivity at low potentials[20], although CO poisoning remains an issue.

In this study, we present the theory-guided discovery of Cu$_x$Sn$_y$ electrocatalysts for the selective reduction of CO$_2$ to formate. A thermodynamic analysis of the reaction energetics using density functional theory (DFT) calculations suggests that Cu–Sn alloys can achieve high formate selectivity through the suppression of hydrogen evolution and CO production, with CuSn$_3$ suggested to be the most promising candidate. We synthesized Cu$_x$Sn$_y$ alloys through a modified co-electrodeposition of Cu and Sn. In situ X-ray absorption studies showed higher oxidation states of Sn in CuSn$_3$ than of Sn in Sn metal at −0.5 V versus RHE, in accordance with theory. Consistent with theoretical predictions, the resultant CuSn$_3$ catalysts exhibit a low potential (−0.5 V versus RHE) in combination with high selectivity (95%) for formate production; these values are among the best of all known non-noble metal systems. The new catalysts also demonstrate excellent stability over the course of a 50 h initial study.

Results

Reaction energetics of Cu, Sn and Cu$_x$Sn$_y$. We investigated the thermochemical reaction energetics of CO$_2$RR and the competing hydrogen evolution reaction (HER) on Sn, CuSn, CuSn$_3$ and Cu using DFT calculations. We used a face-centred cubic (fcc) structure for Cu, and the α-phase for Sn, because these have the lowest formation energies among the different phases[21]. For CuSn, we adopted the hexagonal (point group 6/mmm) structure[22]. For CuSn$_3$, we explicitly investigated a variety of bulk structures and found the hexagonal phase to have the lowest formation energy (Supplementary Table 1). We considered stepped facets, shown previously to be more active for CO$_2$RR, and applied solvation corrections[23]. The structures of the intermediates (H*, COOH*, OCHO* and CO*) are shown in Fig. 1a and Supplementary Fig. 1.

Free energy diagrams (FEDs) for Sn, CuSn, CuSn$_3$ and Cu are presented in Fig. 1b,c. In the case of CO production, COOH* is the relevant intermediate (Fig. 1b)[24]. For formate production, the potential limiting step on Cu and Sn is suggested to be the formation of COOH*, whereas on CuSn and CuSn$_3$ it is suggested to be that of OCHO*[6,25]. The magnitudes of the corresponding thermodynamic limiting potentials |U_L| are summarized in Fig. 1d. In general, we find the theoretical formate activities to be essentially equal (<0.1 eV difference) within uncertainties in the binding energies determined by DFT[26], whereas the CO and HER activities show

[1]Department of Material Science and Engineering, Stanford University, Stanford, CA, USA. [2]SUNCAT Center for Interface Science and Catalysis, Department of Chemical Engineering, Stanford University, Stanford, CA, USA. [3]SUNCAT Center for Interface Science and Catalysis, SLAC National Accelerator Laboratory, Menlo Park, CA, USA. [4]Stanford Synchrotron Radiation Light source, SLAC National Accelerator Laboratory, Menlo Park, CA, USA. [5]Stanford Institute for Materials and Energy Science, SLAC National Accelerator Laboratory, Menlo Park, CA, USA. *e-mail: yicui@stanford.edu
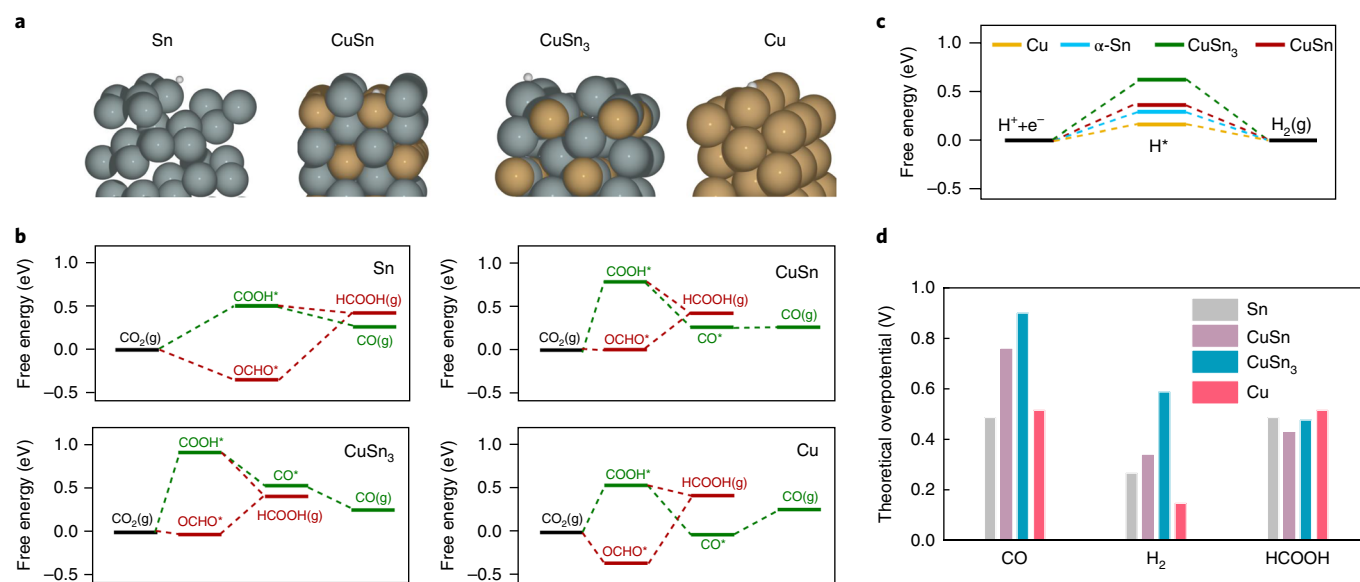
Fig. 1 | DFT calculations on Sn, CuSn, CuSn₃ and Cu. a, Optimized structures of stepped facets of Sn, CuSn, CuSn₃ and Cu with adsorbed H* (see Supplementary Fig. 1 for the configurations of other intermediates). **b,c**, FEDs for CO, HCOOH and H₂ on Sn, CuSn, CuSn₃ and Cu, respectively (note that CO on Sn(211) is physisorbed, so its energy is not included in **b**). **d**, Magnitudes of the theoretical limiting potentials of CO, H₂ and HCOOH production on stepped Sn, CuSn, CuSn₃ and Cu.
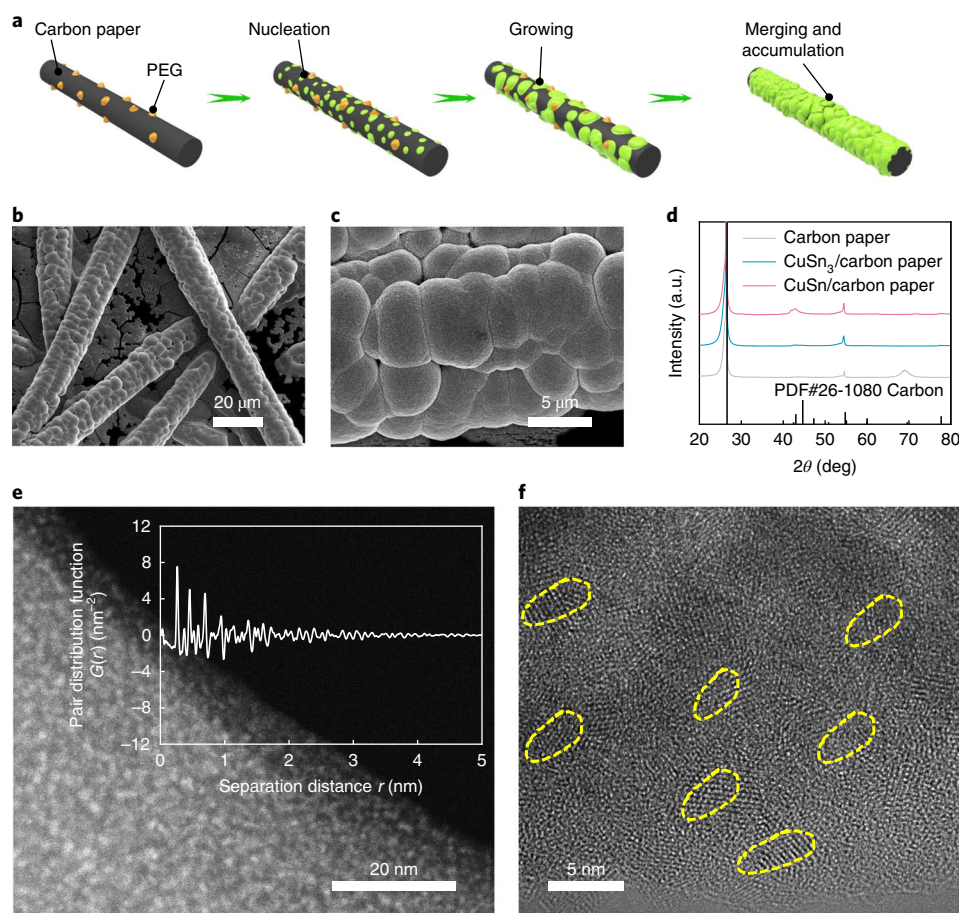
Fig. 2 | Preparation and structural characterization of Cu_xSn_y catalysts. a, Schematic of the process leading to the fabrication of Cu_xSn_y samples. **b,c**, Low- and high-magnification scanning electron microscopy images of CuSn₃ catalysts. **d**, XRD results for carbon paper substrates, CuSn and CuSn₃ electrodes, in which only Bragg peaks from carbon paper were observed. **e,f**, STEM–HAADF (**e**) and high-resolution TEM (**f**) images of CuSn₃ electrodes. Inset (**e**), Pair distribution function peaks for the CuSn₃ diminish at 5 nm because there are no atom–atom pairs separated by more than the particle diameter).

significant variation across the pure metals and alloys. Both CuSn and $CuSn_3$ show higher $|U_L|$ values than Cu and Sn, which suggests the alloying of Cu with Sn to significantly enhance formate selectivity, with $CuSn_3$ suggested to have the lowest activity towards both CO and H_2.

A Bader analysis showed that the alloying of Sn with Cu results in charge transfer from Sn to Cu (Supplementary Fig. 2). In addition, the structures of the alloys are different from both Cu and Sn. Therefore, the origin of the improved selectivity of CuSn and $CuSn_3$ alloys for formate comes from a combination of geometric and electronic effects. The net effect is that the binding of COOH*, H* and OCHO* are all significantly weakened on CuSn and $CuSn_3$, which not only increases the $|U_L|$ for CO and H_2 production, but also changes the relevant intermediates for the formation of formic acid from COOH* to OCHO* (with a smaller $|U_L|$). Therefore, the selectivity for formate on CuSn and $CuSn_3$ is greatly enhanced.

Synthesis and characterization of Cu_xSn_y catalysts. To evaluate the theoretical prediction of high formate selectivity of Cu_xSn_y catalysts, we prepared them by a modified co-electrodeposition process[27] (Fig. 2a). First, we dissolved metal chloride precursors and $(NH_4)_2C_2O_4$ in water to form metal complexes. Polyethylene glycol (PEG2000) was then added to isolate the nucleation of Cu_xSn_y nanocrystals. Since the reduction potentials of Cu^{2+} (−0.55 V versus Ag/AgCl) and Sn^{2+} (−0.85 V versus Ag/AgCl) are different, different potentials were used to co-electrodeposit Cu–Sn alloys (Supplementary Fig. 3). Finally, Cu-doped Sn spheres strung on carbon paper like sugar-coated haws were successfully synthesized (Fig. 2b,c).

From inductively coupled plasma–optical emission spectrometry (ICP–OES) analysis, we determined the molar ratio of Cu:Sn to be 1:3 for Cu–Sn co-electrodeposited at −0.6 V versus Ag/AgCl. X-ray diffraction (XRD) analysis showed that the catalysts lack Bragg peaks and are amorphous or nanocrystalline (Fig. 2d). Scanning transmission electron microscopy (STEM) in high-angle annular dark field (HAADF) mode shows an ~3–5 nm size distribution of nanocrystallines, which is consistent with pair distribution function results[28] (Fig. 2e). Transmission electron microscopy (TEM) further confirmed the size of the $CuSn_3$ particles to be in the range of ~3–5 nm (Fig. 2f). STEM and TEM show that $CuSn_3$ exhibits some nanocrystalline structures embedded in the amorphous structure (Fig. 2e,f).

In situ electronic and structural characterization. To investigate the electronic configuration and structure of the $CuSn_3$ catalysts under operating conditions, we employed an in situ electrochemical flow cell for X-ray absorption spectroscopy (XAS) measurements (Fig. 3a). In the homemade flow cell, electrochemistry was performed using catalysts on carbon paper as a working electrode, a Ag/AgCl reference electrode, a platinum wire counter electrode and a flowing CO_2-saturated 0.1 M $KHCO_3$ solution as the electrolyte (Fig. 3a and Supplementary Fig. 4). All Sn L_3-edge data were collected in fluorescence mode with a seven-element Ge detector (Canberra).

We analysed the Sn L_3-edge position of each compound as this shifts to higher energies with increasing oxidation of Sn[6,29,30]. Sn nanoparticles were used as a control for metallic Sn. SnO was used as a reference for Sn^{2+}. In situ Sn L_3-edge spectra at −0.5 V versus RHE indicate that the Sn within the $CuSn_3$ alloy has an oxidation state of $Sn^{\delta+}$, while pure Sn demonstrated a zero valence and no change in oxidation state at −0.5 V versus RHE (Fig. 3b). At −1.0 V versus RHE, $CuSn_3$ still shows a higher oxidation than zero valence with an edge that shifts to higher energy than metallic Sn (inset of Fig. 3b). The positive charge on Sn is consistent with theoretical calculations; a theoretical Bader analysis of the $CuSn_3$ system suggests that each Sn donates about 0.1 e− to Cu, on average (Supplementary Fig. 2)[31,32].
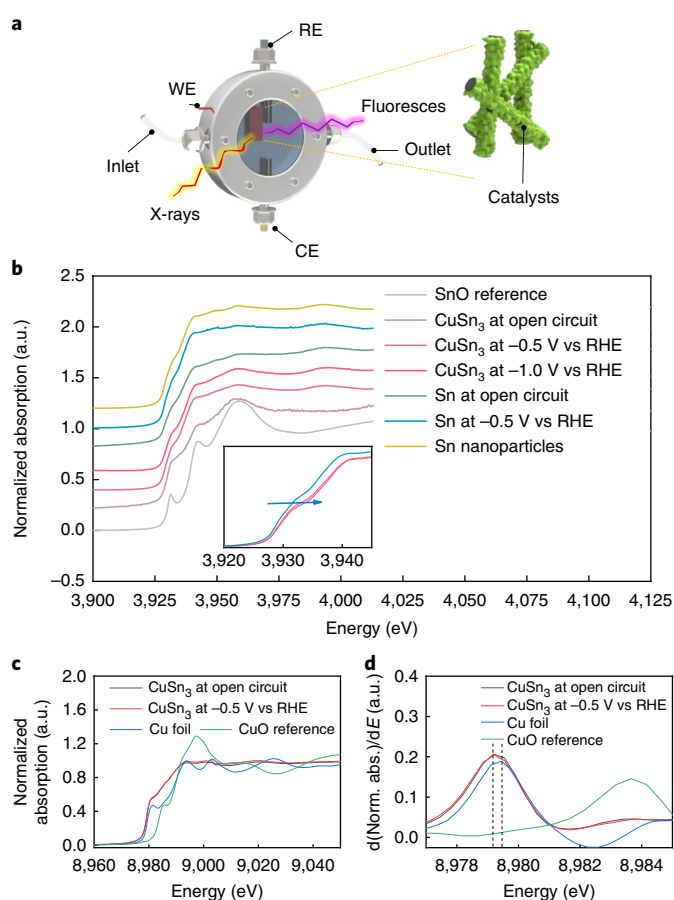
Fig. 3 | In situ observation of the electronic structure of Sn. a, Schematic illustration of the in situ liquid cell experimental set-up. **b,** In situ Sn L_3-edge XANES spectra of Sn nanoparticles, SnO, $CuSn_3$ at −0.5 V versus RHE and −1.0 V versus RHE and Sn at −0.5 V versus RHE. Inset, Enlarged view of the pre-edge energy range of $CuSn_3$ and Sn at operating potentials. **c,** Cu K-edge XANES (**c**) and first derivatives of the normalized Cu K-edge XANES (**d**) spectra of $CuSn_3$ at open circuit and −0.5 V versus RHE. Cu foil and CuO were used as references. WE, working electrode; CE, counter electrode; RE, reference electrode.

The metallic state of Sn in both $CuSn_3$ and pure Sn catalysts was confirmed using extended X-ray absorption fine structure (EXAFS), which showed no peaks assignable to Sn–O bonding in the range 1.5–2.0 Å (Supplementary Fig. 6a)[33]. The white line intensities of the $CuSn_3$ catalysts were slightly larger than that of the Sn foil. This probably originates in electron transfer from Sn to Cu in the $CuSn_3$ catalysts[34,35]. The Sn K-edge suggests that $CuSn_3$ at −0.5 V versus RHE was more positively charged than the Sn metal (Supplementary Fig. 6b), which agrees with the in situ Sn L_3-edge spectra.

Enlarged plots and first derivatives of Cu K-edge X-ray absorption near-edge structure (XANES) spectra are presented in Fig. 3c,d. Cu foil was used as a control for metallic Cu. CuO was used as a reference for Cu^{2+}. The edge positions of $CuSn_3$ catalysts were slightly lower than those of Cu foil, indicating that Cu in $CuSn_3$ had an oxidation state lower than Cu^0. In combination with Sn L_3-edge analysis and our theoretical calculations, this suggests electron donation from Sn to Cu. Cu K-edge EXAFS spectra showed the presence of metallic Cu, and no Cu–O bond was observed (Supplementary Fig. 7). We performed Sn K-edge and Cu K-edge EXAFS fitting for Sn and $CuSn_3$ at open circuit and on applying −0.5 V versus RHE during operating conditions (Supplementary Figs. 8–10).
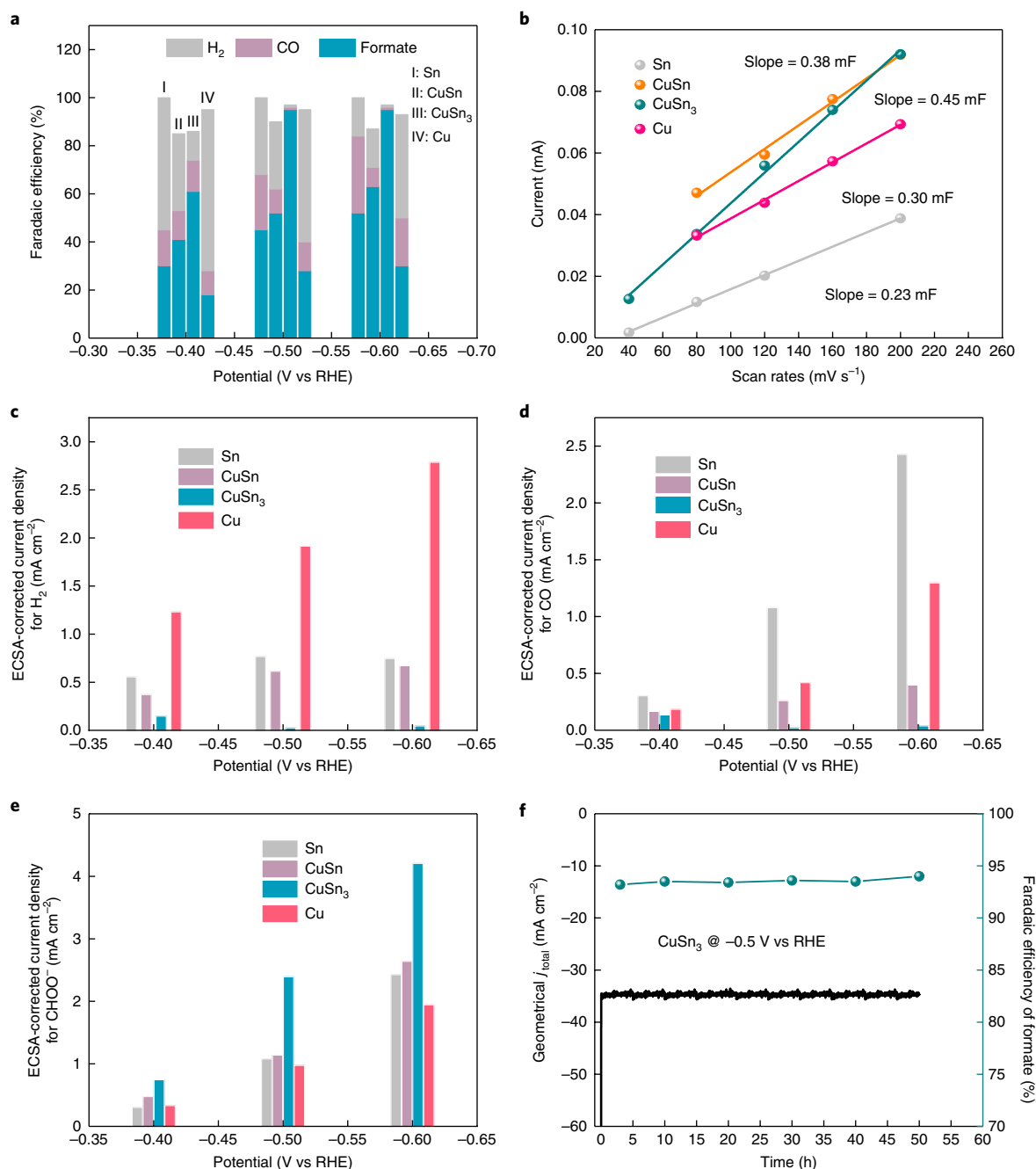
Fig. 4 | Evaluation of CO₂RR catalytic activity by electrochemical measurements. a, Potential dependence of Faradaic efficiencies for CO₂RR on Sn, CuSn, CuSn₃ and Cu electrodes. **b**, ECSA measurements. Orange, blue, pink and grey solid lines represent a linear fit with standard error less than 0.01%. **c–e**, Potential dependence of ECSA-corrected current densities for hydrogen (**c**), carbon monoxide (**d**) and formate (**e**) production. **f**, Stability test of CuSn₃ at −0.5 V versus RHE (green symbols, Faradaic efficiency; black, current density).

The fitting results justify the correlation between the theoretical models and experimental structures.

Evaluation of CO₂RR activity. We explored the CO₂RR activity of Sn, CuSn, CuSn₃ and Sn on carbon paper in CO₂-saturated 0.1 M KHCO₃. In general, we find the experimental trends to be consistent with the thermodynamic analysis of the energetics of the various Cu_xSn_y alloys and controls. Both CuSn and CuSn₃ demonstrated higher selectivity for CO₂ reduction to formate at low overpotentials than either Cu or Sn, and CuSn₃ showed the highest selectivity towards formate, with a Faradaic efficiency of nearly 100% at potentials more negative than −500 mV versus RHE (Fig. 4a and

Supplementary Fig. 12). In contrast, Cu catalysts mainly produced H₂ at these potentials, and Sn catalysts showed lower selectivity towards both CO and formate (Fig. 4a). To further confirm whether CuSn₃ is the optimized composition, we synthesized additional Cu_xSn_y catalysts and explored their catalytic activity (Supplementary Fig. 14). Overall, CuSn₃ catalysts exhibit the best Faradaic efficiency of 95% towards formate and highest j_{COO^-} of 31 mA cm⁻² at −0.5 V versus RHE (Supplementary Fig. 14b).

The activity, normalized by the geometric surface area of the electrodes, does not reflect the intrinsic activity of a catalyst[36]. To evaluate the intrinsic activity of the Cu_xSn_y alloys and controls, we measured the electrochemically active surface area (ECSA) for Sn,

Table 1 | Comparison of catalytic parameters of electrocatalysts for formate production

Samples	Electrolyte	Potential (V versus RHE)	Current density (mA cm⁻²)	FE	Ref.
$CuSn_3$	0.1 M $KHCO_3$	−0.5	33	95%	This work
Sn(S)/Au	0.1 M $KHCO_3$	−0.75	55	93%	Ref. [7]
PdSn/C	0.5 M $KHCO_3$	−0.49	2	99%	Ref. [48]
SnO_x-derived Sn	0.5 M $KHCO_3$	−1.05	12	19%	Ref. [11]
Oxide-derived Pb	0.5 M $KHCO_3$	−1.05	1	95%	Ref. [14]
Sn quantum sheets/GO	0.1 M $KHCO_3$	−1.13	21	85%	Ref. [17]
Partial oxidized Co	0.1 M Na_2SO_4	−0.35	10	90%	Ref. [2]
Pd nanoparticles	0.5 M $KHCO_3$	−0.35	8	90%	Ref. [15]
PdPt alloys	Phospate buffer	−0.4	5	88%	Ref. [20]

CuSn, $CuSn_3$ and Cu (Fig. 4b) and evaluated their ECSA-normalized partial current densities for formate production, hydrogen evolution and CO production (Fig. 4c–e). In accordance with the theoretical thermodynamic analysis, Cu_xSn_y alloys show lower HER and CO production rates, Therefore, they exhibit significantly higher selectivities for formate production than Cu and Sn. In particular, in the case of $CuSn_3$, it suppresses both hydrogen evolution and CO production by one to two orders of magnitude compared to other samples, which results in it having the highest selectivity (Fig. 4c,d).

The trends in activity for HER ($Cu > Sn > CuSn > CuSn_3$) and CO ($Sn > Cu > CuSn > CuSn_3$) also follow those in the theoretical $|U_L|$ (Fig. 1d). In the case of formate, the variations in $|U_L|$ are equal, within the uncertainties of DFT binding energies, and are consistent with the relatively similar (2× variations) ECSA-normalized activity among the various samples.

The incorporation of Cu into Sn materials also enhanced the geometric current densities through an increase in the ECSA (Supplementary Fig. 15 and Table 2). Notably, $CuSn_3$ catalysts exhibited a stable total geometric current density of ~33 mA cm⁻² at a low potential of −0.5 V versus RHE during 50 h of continuous reaction, corresponding to an overpotential of 0.39 V for formate production (Fig. 4f). Time-dependent Sn L_3-edge spectra at −0.5 V versus RHE indicate that the Sn within the $CuSn_3$ alloy has an oxidation state between that of Sn^0 and Sn^{2+}, and no change within several hours (Supplementary Fig. 16). This demonstrated that the Sn site is stable during operating conditions. No obvious changes in the morphology and composition were observed after long-term CO_2RR (Supplementary Figs. 17 and 18). To exclude selectivity and efficiency artefacts owing to the nature of carbon paper, we also evaluated the CO_2RR on a glassy carbon electrode (Supplementary Fig. 19), which showed comparable results. Overall, the selectivity and stability of the $CuSn_3$ alloy outperforms all non-noble metal catalysts reported thus far (Table 1).

Conclusions

We have presented the theory-guided design of Cu–Sn alloys for the selective reduction of CO_2 to formate. Our thermodynamic DFT analysis suggests alloying Cu and Sn to suppress hydrogen and CO generation relative to Cu and Sn, thereby promoting formate selectivity. We report the synthesis of co-deposited Cu_xSn_y alloys, and the structures were characterized in situ under relevant operating conditions. Using in situ X-ray absorption studies of Sn L_3-edges and Cu K-edges, we found electron donation from Sn to Cu in $CuSn_3$ catalysts, resulting in $Sn^{\delta+}$ oxidation states consistent with theory. Cu K-edge and Sn K-edge EXAFS spectra also suggest the formation of a metallic $CuSn_3$ alloy. Our electrochemical results reveal that, in accordance with theoretical predictions, $CuSn_3$ shows significantly improved selectivity (95%) at a low potential (−0.5 V versus RHE). These findings show the importance and potential of the theory-guided rational design of catalysts, and present $CuSn_3$ as

an electrocatalyst with unprecendented activity towards formate as well as stability under reducing conditions.

Methods

DFT calculations. All calculations were carried out with DFT using Quantum ESPRESSO[37], using a plane-wave basis set[38] and ultrasoft pseudopotentials[39,40], interfaced with the atomic simulation environment (ASE)[41]. Plane-wave and density cutoffs of 500 eV and 5,000 eV were used with the BEEF-vdW[42,43] exchange-correlation functional. (4×4×1) Monkhorst–Pack grid K-points were used for (1×3)-Cu(211) and (2×1)-Sn(211), and (3×3×1) grid K-points were used for a (2×2)-(100) surface supercell with a vacuum layer of 14 Å. Dipole corrections were applied in the z direction perpendicular to the slab[44]. The structures were relaxed until the maximal force on the atoms was smaller than −0.05 eV Å⁻¹. DFT calculations were used to probe the energetics along the different CO_2 reduction pathways to hydrogen, formate and carbon monoxide. The computational hydrogen electrode model[45] was adopted to calculate the formation free energies of the intermediates under CO_2 reduction conditions. We included solvation corrections calculated with explicit water models for CO* (0.1 eV) and COOH* (0.25 eV)[23]. Further computational details are included in the Supplementary Methods.

Low coordinated atoms have been found to be generally more active for CO_2RR than flat terrace sites[43,46], so we considered stepped model systems of three-layer (211) facets of Cu and α-Sn and (100) facets of CuSn and $CuSn_3$ (see Supplementary Fig. 1 for the slab and adsorbate structures). The (100) surface of CuSn and $CuSn_3$ can be terminated by either Cu or Sn. Their formation energies are summarized in Supplementary Table 3. The Sn-terminated surface was used for the calculation because its formation energy is 0.06 eV Å⁻² lower on CuSn and 0.01 eV Å⁻² lower on $CuSn_3$(100) than the Cu-terminated surface.

Preparation of Cu_xSn_y. A three-electrode cell was used for the electrodeposition experiments[25]. A Pt electrode was used as a counter electrode. A Ag/AgCl electrode was used as the reference electrode. Carbon paper was used as a working electrode during electrodeposition. Before electrodeposition, the carbon paper substrate was cleaned ultrasonically in 0.1 M HCl, distilled water and isopropanol and then rinsed in distilled water again. The electrochemical deposition experiments were carried out in solutions of 0.01 M $SnCl_2$, 0.01 M $CuCl_2$, 0.06 M $(NH_4)_2C_2O_4$ and 50 ppm PEG2000. To co-electrodeposit CuSn and $CuSn_3$, −0.5 V and −0.6 V versus Ag/AgCl was used. The duration of electrodeposition was 20 h. Cu and Sn controls were synthesized without $SnCl_2$ or $CuCl_2$, respectively.

X-ray absorption measurements. The Sn K-edge spectra were collected at Beamline 11-2 of Stanford Synchrotron Radiation Lightsource (SSRL). Ex situ and in situ Sn-L_3 edges were collected at Beamline 10.3.2 of Advanced Light Source (ALS). The partial fluorescence yield was extracted from all silicon drift detectors (SDDs) by summation of the corresponding metal L emission lines. The X-ray wavelength was monochromatized by a Si(111) double-crystal, fixed-exit monochromator. The intensity of the incident X-ray radiation, I_0, was monitored with a nitrogen-filled ionization chamber. All data were collected in fluorescence mode with a seven-element Ge detector (Canberra). All spectra were aligned according to a glitch in I_0 near the absorption edge. Cu K-edge XANES and EXAFS spectra were collected at Beamline 4-1 at SSRL.

ECSA measurements. To evaluate the effect of surface area, we measured the ECSA for Sn, CuSn, $CuSn_3$ and Cu from the electrochemical double-layer capacitance of the catalytic surface[7,47]. The electrochemical capacitance was determined by measuring the non-Faradaic capacitive current associated with double-layer charging from the scan-rate dependence of cyclic voltammograms (Supplementary Fig. 8).

Electrocatalytic reduction of CO_2. All CO_2 reduction experiments were performed using a three-electrode system connected to an electrochemical

workstation (BioLogic VMP3). Ag/AgCl (with saturated KCl as the filling solution) and platinum mesh were used as reference and counter electrodes, respectively. Electrode potentials were converted to the reversible hydrogen electrode (RHE) reference scale using $E_{RHE} = E_{Ag/AgCl} + 0.197\,V + 0.0591 \times pH$. The electrolyte was 0.1 M KHCO$_3$ saturated with CO$_2$ with a pH of 6.8. The experiments were performed in a gas-tight two-compartment H-cell with compartments separated by an ion exchange membrane (Nafion117). The electrolyte in the cathodic compartment was stirred at a rate of 300 r.p.m. during electrolysis. CO$_2$ gas was delivered into the cathodic compartment at a rate of 20.00 s.c.c.m. and was routed into a gas chromatograph (SRI 8610C).

Product analysis. Gas products were measured by gas chromatography. The gas chromatography column oven was temperature-programmable from ambient to 400 °C with unlimited ramps and holds, and fast cooldown. Argon (Airgas, 99.999%) was used as the carrier gas. The columns led directly to a thermal conductivity detector to quantify hydrogen and a flame ionization detector equipped with a methanizer to quantify carbon monoxide. The partial current densities of carbon monoxide and hydrogen production were calculated from the gas chromatograph peak areas according to the following[3]:

$$j_{CO} = \frac{\text{Peak area}}{\alpha} \times \text{Flow rate} \times \frac{2Fp_0}{RT} \times (\text{Electrode area})^{-1} \tag{1}$$

$$j_{H_2} = \frac{\text{Peak area}}{\beta} \times \text{Flow rate} \times \frac{2Fp_0}{RT} \times (\text{Electrode area})^{-1} \tag{2}$$

where α and β are conversion factors for CO and H$_2$, respectively, based on calibration of the gas chromatograph with standard samples, $p_0 = 1.013$ bar and $T = 300$ K.

Formate was quantified on UI 600 MHz NMR spectrometer. Assuming that two electrons are needed to produce one formate molecule, the Faradaic efficiency was calculated as follows: Faradaic efficiency $= 2F \times n_{formate}/Q = 2F \times n_{formate}/(I \times t)$, where F is the Faraday constant, I is the current, t is the running time and $n_{formate}$ is the total amount of produced formate (in moles).

Data availability
The data supporting the findings of this study are available within the paper and its Supplementary Information and Supplementary Data. Extra data are available from the corresponding author upon reasonable request.

References
1. Lin, S. et al. Covalent organic frameworks comprising cobalt porphyrins for catalytic CO$_2$ reduction in water. *Science* **349**, 1208–1215 (2015).
2. Gao, S. et al. Partially oxidized atomic cobalt layers for carbon dioxide electroreduction to liquid fuel. *Nature* **529**, 68–71 (2016).
3. Liu, M. et al. Enhanced electrocatalytic CO$_2$ reduction via field-induced reagent concentration. *Nature* **537**, 382–386 (2016).
4. Zheng, X. et al. Theory-driven design of high-valence metal sites for water oxidation confirmed using in situ soft X-ray absorption. *Nat. Chem.* **10**, 149–154 (2017).
5. Jhong, H. R., Ma, S. & Kenis, P. J. Electrochemical conversion of CO$_2$ to useful chemicals: current status, remaining challenges and future opportunities. *Nanotechnology* **2**, 191–199 (2013).
6. Feaster, J., Shi, C., Cave, E. R., Nørskov, J. & Jaramillo, T. F. Understanding selectivity for the electrochemical reduction of carbon dioxide to formic acid and carbon monoxide on metal electrodes. *ACS Catal.* **7**, 4822–4827 (2017).
7. Zheng, X., De Luna, P., de Arquer, F. P., Yang, P. & Sargent, E. H. Sulfur-modulated tin sites enable highly selective electrochemical reduction of CO$_2$ to formate. *Joule* **1**, 1–12 (2017).
8. Du, D., Lan, R., Humphreys, J. & Tao Progress in inorganic cathode catalysts for electrochemical conversion of carbon dioxide into formate or formic acid. *J. Appl. Electrochem.* **47**, 661–678 (2017).
9. Reda, T., Plugge, C. M., Abram, N. J. & Hirst, J. Reversible interconversion of carbon dioxide and formate by an electroactive enzyme. *Proc. Natl Acad. Sci. USA* **105**, 10654–10658 (2008).
10. Kuhl, K. P., Cave, E. R., Abram, D. N. & Jaramillo, T. F. New insights into the electrochemical reduction of carbon dioxide on metallic copper surfaces. *Energ. Environ. Sci.* **5**, 7050–7060 (2012).
11. Chen, Y. & Kanan, M. W. Tin oxide dependence of the CO$_2$ reduction efficiency on tin electrodes and enhanced activity for tin/tin oxide thin-film catalysts. *J. Am. Chem. Soc.* **134**, 1986–1989 (2012).
12. Zhu, Q. et al. Efficient reduction of CO$_2$ into formic acid on a lead or tin electrode using an ionic liquid catholyte mixture. *Angew. Chem. Int. Ed.* **55**, 9012–9016 (2016).
13. Li, F., Chen, L., Knowles, G. P., MacFarlane, D. R. & Zhang, J. Hierarchical mesoporous SnO$_2$ nanosheets on carbon cloth: a robust and flexible electrocatalyst for CO$_2$ reduction. *Angew. Chem. Int. Ed.* **56**, 505–509 (2017).
14. Lee, C. H. & Kanan, M. W. Controlling H$^+$ vs CO$_2$ reduction selectivity on Pb electrodes. *ACS Catal.* **5**, 465–469 (2015).
15. Min, X. & Kanan, M. W. Pd-catalyzed electrohydrogenation of carbon dioxide to formate: high mass activity at low overpotential and identification of the deactivation pathway. *J. Am. Chem. Soc.* **137**, 4701–4708 (2015).
16. Zhang, S., Kang, P. & Meyer, T. J. Nanostructured tin catalysts for selective electrochemical reduction of carbon dioxide to formate. *J. Am. Chem. Soc.* **136**, 1734–1737 (2014).
17. Lei, F. et al. Metallic tin quantum sheets confined in graphene toward high-efficiency carbon dioxide electroreduction. *Nat. Commun.* **7**, 12697 (2016).
18. Clark, E. L., Hahn, C., Jaramillo, T. F. & Bell, A. T. Electrochemical CO$_2$ reduction over compressively strained CuAg surface alloys with enhanced multi-carbon oxygenate selectivity. *J. Am. Chem. Soc.* **139**, 15848–15857 (2017).
19. Sun, K., Cheng, T., Wu, L. Z., Goddard, W. A. & Wang, Z. Ultrahigh mass activity for carbon dioxide reduction enabled by gold–iron core–shell nanoparticles. *J. Am. Chem. Soc.* **139**, 15608–15611 (2017).
20. Kortlever, R., Peters, I., Koper, S. & Koper, M. T. Electrochemical CO$_2$ reduction to formic acid at low overpotential and with high Faradaic efficiency on carbon-supported bimetallic Pd–Pt nanoparticles. *ACS Catal.* **5**, 3916–3923 (2015).
21. Jain, A. et al. Commentary: The Materials Project: a materials genome approach to accelerating materials innovation. *APL Mater.* **1**, 11002–11014 (2013).
22. Villars, P. & Calvert, L. D. *Pearson's Handbook of Crystallographic Data for Intermetallic Phases* Vol. 4, 5366 (ASM International, Materials Park, Russell Township, 1991).
23. Peterson, A. A., Abild-Pedersen, F., Studt, F., Rossmeisl, J. & Nørskov, J. How copper catalyzes the electroreduction of carbon dioxide into hydrocarbon fuels. *Energ. Environ. Sci.* **3**, 1311–1315 (2010).
24. Peterson, A. A. & Nørskov, J. K. Activity descriptors for CO$_2$ electroreduction to methane on transition-metal catalysts. *J. Phys. Chem. Lett.* **3**, 251–258 (2012).
25. Yoo, J. S., Christensen, R., Vegge, T., Nørskov, J. & Studt, F. Theoretical insight into the trends that guide the electrochemical reduction of carbon dioxide to formic acid. *ChemSusChem* **9**, 358–363 (2015).
26. Medford, A. et al. Assessing the reliability of calculated catalytic ammonia synthesis rates. *Science* **345**, 197–202 (2014).
27. Bicelli, L. P., Bozzini, B., Mele, C. & D'Urzo, L. A review of nanostructural aspects of metal electrodeposition. *Int. J. Electron. Sci.* **3**, 356–408 (2008).
28. Proffen, K., Page, K., Seshadri, R. & Cheetham A pair distribution function for nanoparticle studies. *Los Alamos Sci.* **30**, 161–164 (2006).
29. Liu, Z., Handa, K., Kaibuchi, K., Tanaka, Y. & Kawai, J. Comparison of the Sn L edge X-ray absorption spectra and the corresponding electronic structure in Sn, SnO and SnO$_2$. *J. Electron. Spectros. Relat. Phenomena* **135**, 155–158 (2004).
30. Gorlin, Y. et al. In situ X-ray absorption spectroscopy investigation of a bifunctional manganese oxide catalyst with high activity for electrochemical water oxidation and oxygen reduction. *J. Am. Chem. Soc.* **135**, 8525–8534 (2013).
31. Henkelman, G., Arnaldsson, A. & Jonsson, H. A fast and robust algorithm for Bader decomposition of charge density. *Comput. Mater. Sci.* **36**, 354–360 (2006).
32. Tang, W., Sanville, E. & Henkelman, G. A grid-based Bader analysis algorithm without lattice bias. *J. Phys. Condens. Matter* **21**, 084204 (2009).
33. Wang, D. et al. Atomic layer deposited coatings to significantly stabilize anodes for Li ion batteries: effects of coating thickness and the size of anode particles. *J. Mater. Chem. A* **2**, 2306–2312 (2014).
34. Horsley, J. A. Relationship between the area of L$_{2,3}$ X-ray absorption edge resonances and the d orbital occupancy in compounds of platinum and iridium. *J. Chem. Phys.* **76**, 1451–1460 (1982).
35. Cramer, S. P., Eccles, T. K., Kutzler, F. W. & Hodgson, K. Molybdenum X-ray absorption edge spectra. The chemical state of molybdenum in nitrogenase. *J. Am. Chem. Soc.* **98**, 1287–1289 (1975).
36. Sun, S., Li, H. & Xu, Z. J. Impact of surface area in evaluation of catalyst activity. *Joule* **2**, 1024–1027 (2018).
37. Giannozzi, P. et al. QUANTUM ESPRESSO: a modular and open-source software project for quantum simulations of materials. *J. Phys. Condens. Matter* **21**, 395502 (2009).
38. Kresse, G. & Furthmuller, J. Efficiency of ab-initio total energy calculations for metals and semiconductors using a plane-wave basis set. *Comput. Mater. Sci.* **6**, 15–50 (1996).
39. Kresse, G. & Hafner, J. Norm-conserving and ultrasoft pseudopotentials for first-row and transition elements. *J. Phys. Condens. Matter* **6**, 8245–8257 (1994).

40. Vanderbilt, D. Soft self-consistent pseudopotentials in a generalized eigenvalue formalism. *Phys. Rev. B* **41**, 7892–7896 (1990).
41. Bahn, S. & Jacobsen, K. An object-oriented scripting interface to a legacy electronic structurecode. *Comput. Sci. Eng.* **2**, 56–67 (2002).
42. Wellendorff, J. et al. Density functionals for surface science: exchange-correlation model development with Bayesian error estimation. *Phys. Rev. B* **85**, 235149 (2012).
43. Liu, X. et al. Understanding trends in electrochemical carbon dioxide reduction rates. *Nat. Commun.* **8**, 15438 (2017).
44. Monkhorst, H. J. & Pack, J. D. Special points for Brillouin-zone integrations. *Phys. Rev. B* **13**, 5188–5192 (1976).
45. Nørskov, J., Rossmeisl, J., Logadottir, A. & Lindqvist, L. Origin of the overpotential for oxygen reduction at a fuel-cell cathode. *J. Phys. Chem. B* **108**, 17886–17892 (2004).
46. Bengtsson, L. Dipole correction for surface supercell calculations. *Phys. Rev. B* **59**, 12301–12305 (1999).
47. Li, C. W., Ciston, J. & Kanan, M. W. Electroreduction of carbon monoxide to liquid fuel on oxide-derived nanocrystalline copper. *Nature* **508**, 504–507 (2014).
48. Bai, X. et al. Exclusive formation of formic acid from CO_2 electroreduction by a tunable Pd–Sn alloy. *Angew. Chem. Int. Ed.* **56**, 12219–12223 (2017).

Author contributions

X.Z. and Y.C. conceived the research and designed the experiments. X.Z., J.T., J.W. and B.L. performed electrochemical measurements. Y.J. and K.C. carried out simulation parts. M.F.T. supervised and designed X-ray absorption and XRD experiments. X.Z., K.L. and H.-G.S. performed the X-ray absorption measurements. H.-G.S. carried out XRD measurements. Y.L. performed TEM measurements. All authors discussed the results and assisted during manuscript preparation.

Competing interests

The authors declare no competing interests.

Additional information

Supplementary information is available for this paper at https://doi.org/10.1038/s41929-018-0200-8.

Reprints and permissions information is available at www.nature.com/reprints.

Correspondence and requests for materials should be addressed to Y.C.